Hearing Research 301 (2013) 168–182

Contents lists available at SciVerse ScienceDirect

Hearing Research

journal homepage: www.elsevier.com/locate/heares

Research paper

Characterizing the ear canal acoustic impedance and reflectance by pole-zero fitting

Sarah R. Robinson*, Cac T. Nguyen, Jont B. Allen

Department of Electrical and Computer Engineering, University of Illinois at Urbana-Champaign, Urbana, IL 61801, USA

ARTICLE INFO

Article history:
Received 31 August 2012
Received in revised form
2 February 2013
Accepted 12 March 2013
Available online 22 March 2013

ABSTRACT

This study characterizes middle ear *complex acoustic reflectance* (CAR) and impedance by fitting poles and zeros to real-ear measurements. The goal of this work is to establish a quantitative connection between pole-zero locations and the underlying physical properties of CAR data. Most previous studies have analyzed CAR magnitude; while the magnitude accounts for reflected power, it does not encode latency information. Thus, an analysis that studies the real and imaginary parts of the data together, being more general, should be more powerful. Pole-zero fitting of CAR data is examined using data compiled from various studies, dating back to Voss and Allen (1994). Recent CAR measurements were taken using the Mimosa Acoustics HearID system, which makes complex acoustic impedance and reflectance measurements in the ear canal over a 0.2–6.0 [kHz] frequency range. Pole-zero fits to measurements over this range are achieved with an average RMS relative error of less than 3% with 12 poles. Factoring the reflectance fit into its *all-pass* and *minimum-phase* components estimates the effect of the residual ear canal, allowing for comparison of the eardrum impedance and admittance across measurements. It was found that individual CAR magnitude variations for normal middle ears in the 1–4 [kHz] range often give rise to closely-placed pole-zero pairs, and that the locations of the poles and zeros in the *s*-plane may systematically differ between normal and pathological middle ears. This study establishes a methodology for examining the physical and mathematical properties of CAR using a concise parametric model. Pole-zero modeling accurately parameterizes CAR data, providing a foundation for detection and identification of middle ear pathologies.

This article is part of a Special Issue entitled "MEMRO 2012".

1. Introduction

1.1. Background

Acoustic reflectance measurements and their clinical applications have been the subject of many recent studies. These studies have shown that power reflectance, the magnitude squared of the *complex acoustic reflectance* (CAR), shows distinct and often systematic variations between pathological and normal middle ears (e.g. Feeney et al., 2003; Allen et al., 2005; Hunter et al., 2010). Studies by Voss et al. (2012) and Nakajima et al. (2012) have investigated the efficacy of reflectance measurements for differential diagnosis of middle ear pathology. Tympanometry and laser doppler vibrometry are the current standards for presurgical differentiation between ossicular fixation, ossicular discontinuity, and third window disorders (Rosowski et al., 2003, 2008); Nakajima et al. concluded that power reflectance performs as well as laser doppler vibrometry, both in combination with audiometry (e.g. air-bone gap measurements), for differential diagnosis of these disorders. This is a valuable result, because CAR measurements can be performed using the United States Food and Drug Administration (FDA) 510(K) cleared HearID system (Mimsosa Acoustics), which, as stated by Nakajima et al. (2012), costs an order of magnitude less than the laser Doppler vibrometer ($\approx 10,000$ vs. 100,000 USD) and requires less training to operate. In another recent study, Voss et al. (2012) systematically manipulated cadaver ears to isolate the effects of various pathologies with differing degrees of severity, and examined the CAR responses. They also concluded that power reflectance may be a strong supplement to audiometry for the diagnosis of certain pathologies.

Abbreviations: CAR, complex acoustic reflectance; TM, tympanic membrane; MSE, mean squared error; RHP, right half plane; LHP, left half plane; SSCD, superior semicircular canal dehiscence

* Corresponding author. 2137 Beckman Institute, MC 251, 405 N. Mathews Ave., Urbana, IL 61801, USA. Tel.: +1 410 458 0042.

E-mail addresses: srrobin2@illinois.edu (S.R. Robinson), tnguyen8@illinois.edu (C.T. Nguyen), jontalle@illinois.edu (J.B. Allen).

0378-5955/$ – see front matter © 2013 Elsevier B.V. All rights reserved.
http://dx.doi.org/10.1016/j.heares.2013.03.004

CAR and impedance are measured at ambient pressure by a probe containing a microphone and loudspeaker, sealed in the ear canal via a foam tip. The probe is calibrated using a multi-cavity least squares procedure to find the Thévenin equivalent parameters of the acoustic source (Allen, 1986). A stimulus is emitted by the probe, and the complex cavity pressure response is measured. From the calibration pressure responses, the acoustic impedance, reflectance, and related quantities (admittance, power reflectance, etc.) may be calculated. The CAR, denoted $\Gamma(\omega)$, is equal to the ratio of the reflected to incident wave pressure at the microphone, located in the ear canal, as a function of frequency ($\omega = 2\pi f$). The magnitude squared of the reflectance, $|\Gamma(\omega)|^2$, represents the relative acoustic power reflected back to the ear canal from the middle and inner ears. The power reflectance is related to conductive hearing functionality and is therefore relevant to clinical assessment of the middle ear (Allen et al., 2005). The complex acoustic impedance $Z(\omega)$ and reflectance $\Gamma(\omega)$, as functions of frequency, are related by

$$\Gamma(\omega) = \frac{Z(\omega)/r_0 - 1}{Z(\omega)/r_0 + 1}, \tag{1}$$

where $r_0 = \rho c/A$ is the estimated *surge resistance*, ρ is the density of air, c is the speed of sound, and A is the area of the ear canal. The 'surge' impedance (Campbell, 1922) is defined as the amplitude of the δ(t) component of the time-domain impedance; because it is a real constant, it is denoted as a *resistance*. It follows that the reflectance is strictly causal (Claerbout, 1985).

The clinical utility of CAR depends on its capacity to discern normal from pathological results, which requires a method for comparing measurements across ears. Direct comparison of CAR is complicated because the residual canal dimensions between the probe tip and *tympanic membrane* (TM) vary across subjects. This uncertainty has a large effect on the reflectance phase and the complex acoustic impedance. The residual ear canal is frequently modeled as a rigid-walled tube of uniform area A and length L. Under this assumption, the relationship between the CAR at the probe and at the TM becomes

$$\Gamma(\omega) = \Gamma_{\mathrm{TM}}(\omega) e^{-j\frac{2L}{c}\omega}. \tag{2}$$

In many cases this is not a realistic model, particularly because the residual ear canal area $A(x)$ varies with distance x (Farmer-Fedor and Rabbitt, 2002). Equation (2) represents a special case of a uniform (constant $A(x)$), lossless canal; a nonuniform, lossless canal would have a more complicated phase dependence on frequency. However, consideration of the CAR magnitude (or the power reflectance $|\Gamma(\omega)|^2$) is highly effective because even when $A(x)$ is nonuniform, the ear canal may be reasonably approximated as lossless, in which case

$$|\Gamma(\omega)| = |\Gamma_{\mathrm{TM}}(\omega)|. \tag{3}$$

Eliminating the variation due to the residual ear canal by using the CAR magnitude or power reflectance allows for comparison across measurements with unknown residual canal dimensions. Thus, the magnitude reflectance is the current diagnostic standard using CAR measurements. The relationship in Eq. (3) was experimentally verified by Voss et al. (2008).

While uncertainty in the residual ear canal volume significantly confounds phase information associated with the eardrum and ossicles, taking the magnitude of the CAR eliminates this relevant information entirely. It follows that a holistic analysis of the complex data could be more powerful and generalizable if the canal effect were accounted for in a rigorous manner, without eliminating all phase data. This study seeks to develop such a method for concise parametric characterization of CAR measurements, with the ultimate goal of improving differential diagnosis of middle ear pathology. This is accomplished by fitting poles and zeros to the complex data. It is important to note that this work is primarily intended to aid in middle ear modeling efforts and automated diagnosis of pathologies; it is not our intention to introduce a raw pole-zero diagnosis into the clinic.

1.2. Pole-zero fitting

Poles and zeros may be expressed in terms of a rational polynomial fraction, as the roots of the denominator and numerator, respectively. Such a function will have the form

$$\begin{aligned}\widehat{F}(s) &= \frac{b_{N_z}s^{N_z} + b_{N_z-1}s^{N_z-1} + \ldots + b_1 s + b_0}{s^{N_p} + a_{N_p-1}s^{N_p-1} + \ldots + a_1 s + a_0} \\ &= b_{N_z}\frac{\prod_{i=1}^{N_z}(s - z_i)}{\prod_{i=1}^{N_p}(s - p_i)},\end{aligned} \tag{4}$$

where s is the complex angular frequency variable ($s = \sigma + j\omega$), a_i and b_i are the polynomial coefficients, N_p is the number of poles, N_z is the number of zeros, p_i are the poles, and z_i are the zeros (Van Valkenburg, 1964). For our application, the relative order is constrained to $|N_z - N_p| \leq 1$ by the fitting procedure (Appendix A). Poles and zeros are a familiar concept regarding impedance; considering Eq. (1), the reflectance must also have poles and zeros via a simple algebraic transformation. Thus, $\widehat{F}(s)$ may be a fit to the impedance Z, the reflectance Γ, or some other simple algebraic transformation of the data.

Some example CAR measurements (dots) and pole-zero fits (lines) are shown in Fig. 1 for two standard artificial ear simulators, the B&K 4157 (black) and the DB-100 (gray). These measurements are from Voss and Allen (1994). Each fit is performed on reflectance domain data ($\Gamma(\omega)$) with $N_p = N_z = 6$; the B&K 4157 fit has a RMS relative error of 1.7%, and the DB-100 fit has a RMS relative error of 2.9%. Reflectance and impedance magnitude vs. frequency (Fig. 1a, b), and phase vs. frequency (Fig. 1c, d), are shown for both couplers. The impedance is normalized by the estimated surge resistance, r_0. Effects of the residual simulator ear canals are particularly noticeable in the reflectance phase and normalized impedance magnitude. Considering the reflectance phase (Fig. 1c), the DB-100 has a much flatter phase across frequency than the B&K 4157, indicating less delay and thus a shorter residual canal. The normalized impedance magnitude of the B&K 4157 shows a high frequency notch, while the normalized impedance magnitude of the DB-100 does not. This deep notch is due to the ear canal 'standing wave' between the TM and the probe tip (Scheperle et al., 2008; Withnell et al., 2009). The absence of such a notch in the DB-100 impedance magnitude indicates a shorter distance between the probe tip and TM; such a notch may still exist, but at a higher frequency outside of the measured range. Finally, considering the impedance magnitude and phase, the B&K 4157 ear canal impedance becomes mass dominated at high frequencies (beyond the standing wave frequency) while the DB-100 impedance does not.

According to Voss and Allen (1994), the reflectance magnitude of the DB-100 ear simulator best resembles that of their ten human ear average below 4 [kHz], but the B&K 4157 is a better match to the average for frequencies up to 10 [kHz]. Considering Fig. 1a, the B&K 4157 reflectance magnitude is close to one at low frequencies, has a broad minimum from about 1 to 4 [kHz], and rises again at high

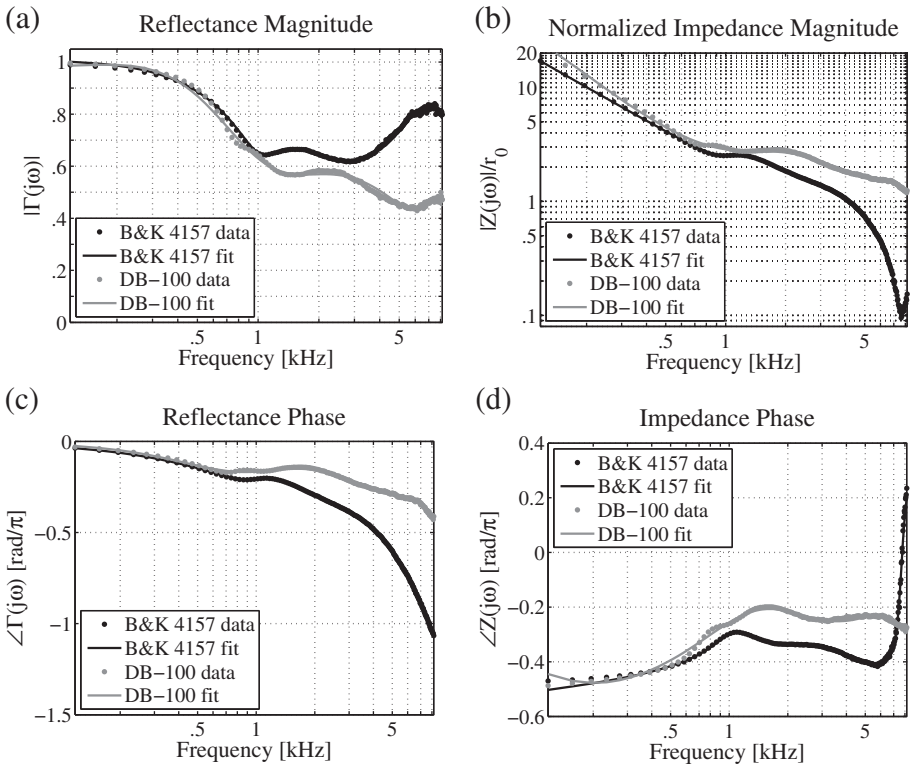

Fig. 1. Standard ear simulater measurements from Voss and Allen (1994). (a) Reflectance magnitude $|\widehat{\Gamma}(j\omega)|$, (b) normalized impedance magnitude $|\widehat{Z}(j\omega)|/r_0$, (c) reflectance phase $\angle\widehat{\Gamma}(j\omega)$, (d) impedance phase $\angle\widehat{Z}(j\omega)$. Example measured data (dots) and pole-zero fit (lines) are shown for the B&K 4157 (black) and the DB-100 (gray). The fits were performed in the reflectance domain over 0.1–8.2 [kHz], yielding 6 poles and 6 zeros for each fit. The B&K 4157 fit has a RMS relative error of 1.7%, and the DB-100 fit has a RMS relative error of 2.9%. The reflectance magnitude (a) of the B&K 4157 is more similar to an average normal ear across the entire frequency range than the DB-100. The DB-100 exhibits a much shorter ear canal behavior than the B&K 4157 considering the impedance magnitude (b) and the reflectance phase (c).

frequencies; this is also similar to the average results obtained by Rosowski et al. (2012), among others. However, the reflectance magnitude of the DB-100 does not share this high frequency behavior, instead continuing to decrease above 4 [kHz]. Thus, the B&K 4157 measurement is a better standard for comparison of complex pole-zero fits, and will be used in this paper to represent an average normal ear. It is important to note that while the average magnitude reflectance of normal middle ears has a broad, flat minimum from about 1 to 4 [kHz], individual ears have variable fine-structure minima and maxima in this range (Rosowski et al., 2012; Allen et al., 2005). These intersubject variations are typically due to anatomical differences across ears, including properties of the TM, ossicles, middle ear cavities and inner ear load (Voss et al., 2000; Aibara et al., 2001; Rosowski et al., 2012).

Fig. 2 shows the poles and zeros that produce the fit to the B&K 4157 shown in Fig. 1. Fig. 2a shows the poles and zeros of the reflectance fit $\widehat{\Gamma}(s)$ and Fig. 2b shows the poles and zeros of the normalized impedance fit $\widehat{Z}(s)/r_0$, which have been calculated from the fitted reflectance domain poles via Eq. (1). Notice that in both domains the poles and zeros have complex conjugate symmetry (those in the upper half s-plane mirror those in the lower half s-plane); this is a necessary condition for the polynomial coefficients in Eq. (4) to be real. With relation to the magnitude and phase response, the $\omega = Im\{s\}$ location of a pole or zero typically determines the frequency region in which it has the largest effect, and the $\sigma = Re\{s\}$ component of a pole or zero is related to the damping. Poles and zeros with smaller damping, which lie closer to the ω axis, have a larger effect on the fitted magnitude and phase responses. Throughout this presentation, pole-zero locations will be plotted as $s/(2\pi)$, such that the frequency axis $f = \omega/(2\pi)$ may be referenced to the frequency axes of the magnitude and phase responses.

Considering the poles and zeros of $\widehat{\Gamma}(s)$ in Fig. 2a, the pole-zero pair labeled a (with conjugate a^*) seems to characterize the first minimum of the magnitude reflectance at 1 [kHz] (Fig. 1a), while the zero at b (b^*) and the pole at c (c^*) correspond to its high-frequency behavior. Considering the pole–zero plot of the normalized impedance $\widehat{Z}(s)/r_0$ (Fig. 2b), note the solitary pole, labeled d, on the real axis approximately at the origin. This pole is actually in the *right half s-plane* (RHP), with a relatively small value of $\sigma/(2\pi) = 9$ [Hz], causing the impedance fit to be unstable. Because its $|\sigma|$ value is small, pole d is functionally at the origin; such small instabilities in the impedance can occur when fitting reflectance domain data, and will be discussed at length in Section 2.1.2. Because it is approximately at the origin, the pole at d characterizes the stiffness of the impedance below 1 [kHz]; it has a stronger effect on $|\widehat{Z}(j\omega)|/r_0$ (Fig. 1b) than the other zeros and poles on the real axis, as it has the smallest σ value. Thus the pole-zero fits may be used to model some physics of CAR and impedance measurements.

It is important to note that pole-zero fitting of CAR data cannot be accomplished by autoregressive moving-average (ARMA) modeling methods (e.g. Recio-Spinoso et al., 2011), because the time domain signal $\gamma(t) = \mathcal{F}^{-1}\{\Gamma(\omega)\}$ (where $\mathcal{F}^{-1}$ denotes the inverse Fourier transform) is not very precise. CAR is measured as a function of frequency, and measurement noise below 100 or 200 [Hz] typically prevents the accurate calculation of an inverse FFT. Instead, a method developed by Gustavsen and Semlyen (1999) is used to fit CAR data directly in the frequency domain. This procedure finds a rational approximation of the data as a function of complex frequency, using their 'vector fitting' method. Such pole-zero fits capture magnitude and phase characteristics of CAR measurements with low RMS relative error and a small set of

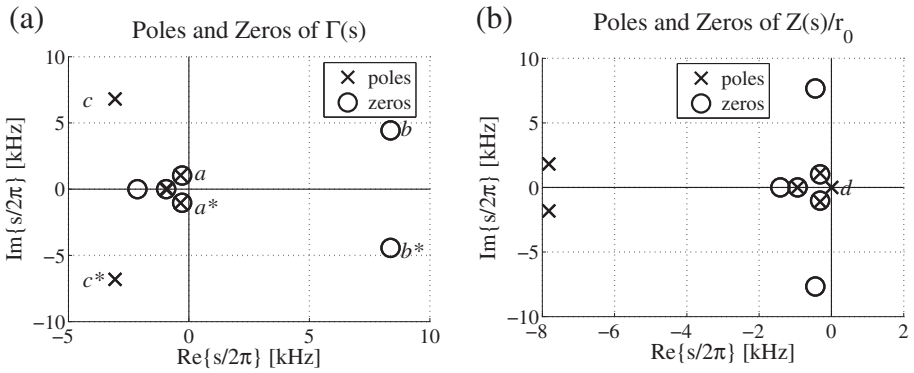

Fig. 2. Pole-zero fit of the B&K 4157 measurement from Voss and Allen (1994). (a) Poles and zeros of $\widehat{\Gamma}(s)$, (b) poles and zeros of $\widehat{Z}(s)/r_0$. Note that there are two closely-spaced poles on the real axis in (a), though they appear to overlap on this scale. The fit was performed in the reflectance domain over 0.1–8.2 [kHz], and the impedance domain poles and zeros were calculated via Eq. (1). This pole-zero fit produces the curves shown in Fig. 1. The pole-zero pair labeled *a* (a) appears to characterize the first minimum of $|\widehat{\Gamma}(j\omega)|$ (Fig. 1a), and the pole at *d* (b) appears to characterize the low-frequency stiffness of $|\widehat{Z}(j\omega)|$ (Fig. 1b).

parameters. The fitting procedure is described next, followed by our results and their diagnostic implications.

2. Methods

2.1. Fitting CAR data

The CAR data sets examined in this paper were compiled from previous studies. A population of normal ears was drawn from Voss and Allen (1994) and Rosowski et al. (2012). Fourteen CAR measurements of ten ears (four retest measurements) were collected in vivo up to 15 [kHz] by Voss and Allen, using a measurement system described in their paper. The B&K 4157 and DB-100 ear simulator measurements shown in Fig. 1 were also collected in that study. Fifty-eight CAR measurements (and 58 retest measurements) were collected in vivo over a frequency range of 0.2–6 [kHz] by Rosowski et al., using the Mimosa Acoustics HearID system. These 58 "strictly normal" ears met specific audiometric criteria in order to be included in the study.

Pathological and cadaver measurements were drawn from Nakajima et al. (2012) and Voss et al. (2012). The Nakajima et al. (2012) CAR measurements were collected in vivo from patients with confirmed stapes fixation due to otosclerosis, ossicular discontinuity, and superior semicircular canal dehiscence. The Voss et al. (2012) CAR measurements were collected from cadaver preparations, which were manipulated to simulate static pressure disorders in the middle ear cavity (positive and negative), middle ear fluid, fixed stapes, disarticulated incudo-stapedial joints, as well as TM perforations. Additionally, the cadaver ears were measured in their 'normal' (unmodified) state. These data were also collected using the Mimosa Acoustics HearID system.

2.1.1. Pole-zero fitting procedure

Rational approximations to the CAR data as a function of frequency ($\omega = 2\pi f$) were calculated using a vector fitting procedure developed by Gustavsen and Semlyen (1999). $\widehat{F}(s)$, where $s = \sigma + j\omega$ is the complex angular frequency variable, will be used to denote the complex frequency domain fit, and $F(\omega)$ will be used to denote the measured complex frequency domain data. It is important to note that the data is only available as a function of ω, thus the data is related to the fitted function by $F(\omega) \approx \widehat{F}(s)|_{s=j\omega}$; in words, when $\widehat{F}(s)$ is evaluated along the ω axis of the complex s-plane, it approximates the observed data. Because the middle ear is not a lossless system, the poles and zeros of the fit are typically located off the ω axis (have non-zero σ values related to the damping). Thus $\widehat{F}(s)|_{s=j\omega}$ typically has minima and maxima instead of zero and infinite values.

The data (e.g. the complex reflectance $\Gamma(\omega)$, impedance $Z(\omega)$, or admittance $Y(\omega) = 1/Z(\omega)$) is fit to a residue expansion of the form

$$\widehat{F}(s) = \sum_{i=1}^{N_p} \frac{C_i}{s - A_i} + D + Es, \tag{5}$$

where the constants D and E are real quantities, while the constant poles and residues, A_i and C_i, are either real or occur in complex conjugate pairs. Note that if E and D are non-zero, the numerator order (N_z, Eq. (4)) is one greater than the denominator order ($N_z = N_p + 1$). Similarly, if E is zero and D is non-zero the numerator and denominator orders are equal ($N_z = N_p$), and if both D and E are zero the numerator order is one less than the denominator order ($N_z = N_p - 1$). Equation (5) is nonlinear in its unknowns, because the unknown poles A_i appear in the denominator. Since the poles and zeros of a 1-port network impedance are restricted to first order, with a relative order of $|N_z - N_p| \leq 1$, the functional form of Eq. (5) is sufficient for fitting impedance domain data (Van Valkenburg, 1964). The reflectance does not have the same constraints, but given its relationship to impedance (Eq. (1)) we assume it will also fit well to this form. It is important to note that while the total number of parameters may seem daunting, there are typically fewer 'degrees of freedom' than it seems, because the complex poles and zeros are constrained to come in complex conjugate pairs. For instance, if a fit has twelve poles and ten of them are complex, there are only seven 'degrees of freedom' related to the poles, because five (half) of the complex poles are constrained by conjugate symmetry. This constraint is preserved under the transformation in Eq. (1).

The vector fitting procedure is a two step process, which converts a nonlinear least squares problem to a linear least squares problem by introducing an unknown scaling function with known poles (Gustavsen and Semlyen, 1999). This procedure is described at length in Appendix A. Given a fixed number of poles, the algorithm converges very rapidly, usually within a few iterations. The algorithm may be re-run with an increasing number of poles, until some error criterion is met. For some measurements, the fitting procedure may return a set of poles and zeros with nearly overlapping pole-zero pairs, due to small extrema from measurement noise. Such pairs may be considered to 'overfit' the data, and it is often possible to eliminate them from the fit without causing an appreciable increase in the fitting error. For the remainder of this presentation, goodness of fit will be described using a *mean squared error* (MSE) metric, in decibels, relative to the L2 norm of the signal:

$$\text{MSE [dB]} = 10\log_{10}\left[\frac{\sum\left|F(\omega)-\widehat{F}(j\omega)\right|^2}{\sum|F(\omega)|^2}\right]. \quad (6)$$

A MSE of −30 [dB] corresponds to a RMS relative error of about 3%.

2.1.2. Domain of fitting

An error analysis of the fitting procedure is given in Fig. 3. Average MSE vs. pole order is plotted for pole-zero fits of two data sets of normal middle ears in different domains. The impedance (Z), admittance (Y), and reflectance (Γ) domains are examined. Fig. 3a shows the average MSE for fits of 14 normal ear measurements made by Voss and Allen (1994) over 0.1–10 [kHz]. Fig. 3b shows the average MSE for fits of 112 normal ear measurements made by Rosowski et al. (2012) over 0.2–6 [kHz]. Error bars show ±1 standard deviation of the MSE for a given data set and fitting domain. Considering Fig. 3a and b, the fit error saturates between about 10 and 20 poles, beyond which the algorithm begins to fit the measurement noise; this behavior is best captured by the admittance and reflectance domain curves in Fig. 3b, where the error improves by 15 [dB] between 4 and 20 poles, and by less than 5 [dB] between 20 and 60 poles. Fig. 3a shows higher average MSEs than Fig. 3b. This is primarily because the Voss and Allen (1994) measurements were fit over a larger frequency range, which includes more noise than the Rosowski et al. (2012) measurement range. In Fig. 3a, impedance domain fitting performs better than admittance domain fitting, and vice versa in Fig. 3b, due to the frequency range of the fit and measurement noise. Because of the typical shape of the impedance response (e.g. Fig. 1b), low frequency noise has a larger effect on error in the impedance domain, and high frequency noise has a larger effect on error in the admittance domain. There are differing amounts of low and high frequency noise over the 0.1–10 [kHz] and 0.2–6 [kHz] ranges, causing differences in impedance domain error relative to admittance domain error.

Considering Fig. 3, the fitting procedure consistently performs best in the reflectance domain. Additionally, for diagnostic applications it may be desirable to have the best possible fit to the magnitude reflectance, which has shown the greatest promise for detecting middle ear pathologies. While the impedance magnitude and phase are both dominated by the ear canal response, in the reflectance domain only the phase is significantly affected by the ear canal (e.g. Eq. (2)). Additionally, the dynamic range of the reflectance is much smaller than that of the impedance, typically spanning less than 10 [dB], whereas the impedance may span 20–40 [dB] (1–2 orders of magnitude). Due to the nature of the least squares procedure, small magnitude data points of $Z(\omega)$ inadvertently receive less emphasis in the fitting procedure than data points with larger magnitude. Thus, fitting to the impedance may provide a better approximation to the low frequency data (where the magnitude is large, as in Fig. 1b), but will yield a relatively poorer fit in the mid-frequency region of the reflectance magnitude, where individually varying minima and maxima occur for normal middle ears. To characterize the reflectance for a given ear, it may be useful to capture these fluctuations. Due to the smaller dynamic range of the reflectance, fitting the data in the reflectance domain gives approximately equal weight to the error across frequencies. Fitting 112 measurements over the 0.2–6 [kHz] range in the reflectance domain, an average MSE of −33.4 [dB] (2.1% RMS relative error with a standard deviation of 0.7%) is achieved with 12 poles for 18 iterations of the fitting algorithm. Fitting the data over a larger frequency range typically requires more poles.

Considering all measurements from the Rosowski et al. (2012) and Nakajima et al. (2012) studies, it was found that reflectance domain fits usually yield values of E (Eq. (5)) that are close to zero. Typically, $|E|$ is very small for fits to both normal and pathological CAR measurements, on the order of 10^{-5} for fits with $N_p < 20$. For higher pole orders there is more variation in the value of $|E|$, which is to be expected as the number of fitting parameters increases. Average $|E|$ values are similar for normal and pathological data sets, indicating that this is a property of reflectance measurements and not a property of middle ear functionality. These results suggest that E should be forced to zero when fitting in the reflectance domain, enforcing a relative pole-zero order of $N_p \geq N_z$. For most fits, forcing E to be zero has a negligible effect on the error; often this effect may be remedied by adding a few more poles. However, the average value of $|D|$ is on the order of 1 for fits with $N_p < 20$. For instance, when fitting 112 measurements of normal ears from Rosowski et al. (2012) with $N_p = N_z = 12$, the average magnitude of D is 0.8 with a standard deviation of 0.4. Thus, it seems necessary to allow D to be non-zero when fitting in the reflectance domain, resulting in a relative pole-zero order of $N_p = N_z$. While it may not be obvious, this is a significant conclusion due to the physical meaning of D, as we will discuss in Section 4.2.

When the fitting procedure is performed in the reflectance domain, all fits to $\Gamma(\omega)$ are stable (all poles are in the *left half s-plane* (LHP)) because stability is enforced by the algorithm (see Appendix A). However, when the fit is transformed to the impedance domain by the relation in Eq. (1), stability is not ensured. If E is allowed to be non-zero, out of the fits performed to 112 measurements of $\Gamma(\omega)$ over 0.2–6 [kHz] (Rosowski et al., 2012) with a −30 [dB] MSE tolerance, no fits are stable when transformed to the impedance domain. With E forced to zero and all other conditions the same, 59 fits are stable in the impedance domain. All of these fits are also minimum-phase in the impedance domain, meaning that the zeros of $\widehat{Z}(s)/r_0$ reside in the LHP as well as the poles, ensuring that both

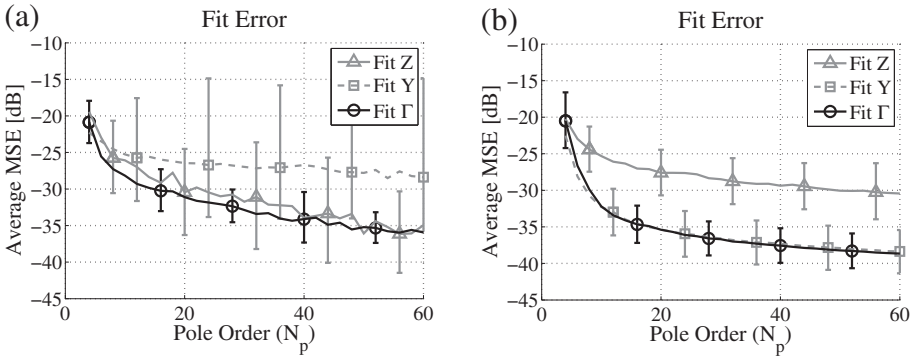

Fig. 3. Fit error evaluation across the impedance (Z), admittance (Y) and reflectance (Γ) domains for different data sets (18 iterations of the fitting algorithm). Lines show the average MSE [dB] vs. pole order (N_p) for each domain, with error bars indicating one standard deviation. (a) 14 measurements of normal ears (Voss and Allen, 1994) fit over the 0.1–10 [kHz] range, (b) 112 measurements of normal ears (Rosowski et al., 2012) fit over the 0.2–6 [kHz] range. Fitting measurements in the Γ domain achieves the lowest fitting error overall.

the impedance and admittance are causal and stable. Of the 53 remaining fits to $\Gamma(\omega)$ that are unstable when transformed to the impedance domain, 46 have a single pole of $\widehat{Z}(s)/r_0$ that lies on the real axis in the RHP causing the instability; that pole has a mean value of $\sigma/2\pi = 17.8$ [Hz], with a standard deviation of 12.2 [Hz]. Thus, for these 46 fits, the unstable pole is approximately at the origin of the s-plane, characterizing the low frequency stiffness of $Z(\omega)$ for a normal middle ear. The remaining 7 fits to $\Gamma(\omega)$ which are unstable in the impedance domain have higher pole orders and may need more careful attention during the fitting procedure (e.g. the data is noisy). Note that the impedance should be minimum-phase, and it should also have the positive real property, $\mathrm{Re}\{Z(\omega)\} \geq 0$ for all frequencies, assuming the system is passive (Brune, 1931). Due to noise, some CAR measurements have $|\Gamma(\omega)| > 1$, corresponding to $\mathrm{Re}\{Z(\omega)\} < 0$ for some ω (Van Valkenburg, 1964). Typically, all fits to these measurements will also have $|\widehat{\Gamma}(j\omega)|>1$.

2.2. Comparing complex fits

Considering the CAR instead of its magnitude re-introduces the problem of comparing across measurements, because the residual ear canal introduces uncontrolled variation in the complex response (due to varying probe-TM distance, and canal area). This effect is difficult to extract, particularly because the limited high frequency range of the measurements does not allow for a good estimate of any pure delay in the ear canal. Even though measurements are available to 15 [kHz] for the Voss and Allen (1994) study, there is high frequency noise in the data that makes it difficult to accurately estimate the distance L from the probe to the TM (this point was previously made in their 1994 publication).

Under the assumption that the ear canal is lossless, and the rest of the middle ear system has loss, the reflectance may be factored such that the residual ear canal effect is approximately removed. Using the Weiner factorization technique

$$\widehat{\Gamma}(s) = \widehat{\Gamma}_{mp}(s)\widehat{\Gamma}_{ap}(s), \tag{7}$$

where $\widehat{\Gamma}_{mp}(s)$ is the *minimum-phase* component and $\widehat{\Gamma}_{ap}(s)$ is the *all-pass* component of the pole-zero fit $\widehat{\Gamma}(s)$, it is possible to preserve the magnitude reflectance while removing variable residual canal delay.

By definition, it is required that all poles and zeros of a *minimum-phase* function lie in the LHP. To construct the minimum-phase component $\widehat{\Gamma}_{mp}(s)$, we must factor a component out of $\widehat{\Gamma}(s)$ that accounts for all zeros that lie in the RHP (if the fit was performed in the reflectance domain, all poles will be constrained to the LHP by the fitting algorithm). Let the function $\widehat{\Gamma}_{\mathrm{LHP}}(s)$ contain all the poles and zeros of $\widehat{\Gamma}(s)$ that lie in the LHP; let $N_{z,\mathrm{RHP}}$ be the number of RHP zeros of $\widehat{\Gamma}(s)$, with values q_i. The reflectance fit may be factored as follows:

$$\begin{aligned}\widehat{\Gamma}(s) &= \widehat{\Gamma}_{\mathrm{LHP}}(s)\prod_{i=1}^{N_{z,\mathrm{RHP}}}(s-q_i)\\ &= \widehat{\Gamma}_{\mathrm{LHP}}(s)\prod_{i=1}^{N_{z,\mathrm{RHP}}}(s-q_i)\frac{(s+q_i^*)}{(s+q_i^*)}\\ &= \underbrace{\left[\widehat{\Gamma}_{\mathrm{LHP}}(s)\prod_{i=1}^{N_{z,\mathrm{RHP}}}\left(s+q_i^*\right)\right]}_{\widehat{\Gamma}_{mp}(s)}\underbrace{\left[\prod_{i=1}^{N_{z,\mathrm{RHP}}}\frac{(s-q_i)}{\left(s+q_i^*\right)}\right]}_{\widehat{\Gamma}_{ap}(s)}.\end{aligned} \tag{8}$$

Considering Eq. (8), overlapping poles and zeros are introduced in the LHP at $s = -q_i^*$. Grouping the terms, a component with LHP poles and RHP zeros symmetrically placed about the ω axis emerges. This is called the *all-pass* component, because its magnitude $|\widehat{\Gamma}_{ap}(j\omega)|$ is 1 for all frequencies in the fitting range; it passes all frequencies with no attenuation. The factorization required to form the all-pass component is unique. The remaining terms contain only poles and zeros in the LHP, and form the minimum-phase factor $\widehat{\Gamma}_{mp}(s)$. When working with poles and zeros, this factorization requires no additional calculations.

An example of this factorization is shown in Fig. 4. Fig. 4a shows the all-pass component and Fig. 4b shows the minimum-phase component of the reflectance fit shown in Fig. 2a (the B&K 4157). Note that Fig. 4b shows only the northwest quadrant of the s-plane. This style of plotting will be used for all $\widehat{\Gamma}_{mp}(s)$ results; though limited to one quadrant of the LHP, it completely describes the set of poles and zeros for a given fit. By definition, $\widehat{\Gamma}_{mp}(s)$ only has poles and zeros in the LHP. Thus, a logarithmic σ axis may be used for the LHP (northwest and southwest quadrants), on which the large dynamic range of σ values may be more easily viewed. Because the southwest quadrant contains only complex conjugates of the poles and zeros in the northwest quadrant, it does not need to be shown. Considering Fig. 2a, the zeros at b and b^* correspond to the q_i's in Eq. (8). To factor the fit, overlapping poles and zeros are introduced at $-b^*$ and $-b$, respectively; the zeros are assigned to $\widehat{\Gamma}_{mp}(s)$ (Fig. 4b), and the poles are assigned to $\widehat{\Gamma}_{ap}(s)$ (Fig. 4a) along with the RHP zeros of $\widehat{\Gamma}(s)$. Note how the poles and zeros of $\widehat{\Gamma}_{ap}(s)$ are symmetrically placed about the ω axis, such that the poles and

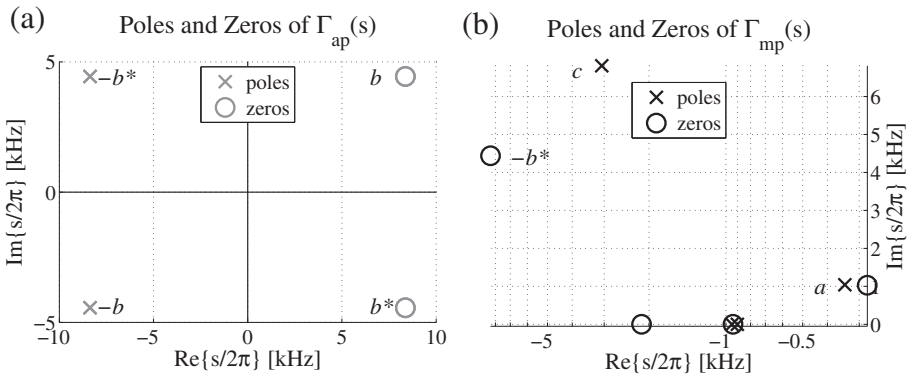

Fig. 4. An example of the Weiner factorization (Eq. (7)), using the B&K 4157 pole-zero fit (Fig. 2a). (a) Poles and zeros of $\widehat{\Gamma}_{ap}(s)$, (b) poles and zeros of $\widehat{\Gamma}_{mp}(s)$. Note that by definition $\widehat{\Gamma}_{mp}(s)$ has no poles or zeros in the right half s-plane, thus the fit is completely described by northwest quadrant of the s-plane (shown in (b)). All poles and zeros in (b) with non-zero $\omega/(2\pi)$ values have complex conjugates in the southwest quadrant, not shown.

zeros at b, b^*, $-b^*$ and $-b$ are constrained by both complex conjugation and all-pass symmetry.

The minimum-phase and all-pass factors have the following properties:

$$\left|\widehat{\Gamma}_{mp}(j\omega)\right| = \left|\widehat{\Gamma}(j\omega)\right| \tag{9}$$

$$\left|\widehat{\Gamma}_{ap}(j\omega)\right| = 1 \tag{10}$$

$$\angle\widehat{\Gamma}_{mp}(j\omega) + \angle\widehat{\Gamma}_{ap}(j\omega) = \angle\widehat{\Gamma}(j\omega). \tag{11}$$

The reflectance magnitude is maintained in the minimum-phase component of the fit, while the component of the reflectance that is uniformly lossless across the frequency range of the fit, including any pure delay, is accounted for in the all-pass component. Because the factors are multiplied, their phases add.

Assuming negligible losses in the ear canal, we may approximate the residual ear canal contribution to the reflectance as the all-pass component $\widehat{\Gamma}_{ap}(s)$. In some cases, the all-pass component of the factorization has an approximately linear phase (constant group delay), resulting in a robust estimate $\widehat{L}$ of the ear canal length according to Eq. (2). From this equation, the constant group delay may be calculated as

$$\tau_{ap}(\omega) = -\frac{\mathrm{d}\phi_{ap}(\omega)}{\mathrm{d}\omega} \approx \frac{2\widehat{L}}{c}, \tag{12}$$

where $\phi_{ap}(\omega)$ is the phase of $\widehat{\Gamma}_{ap}(j\omega)$. If $\tau_{ap}(\omega)$ is frequency dependent, a frequency independent delay may be estimated by taking its minimum over the measured frequency range. When $\widehat{\Gamma}_{ap}(s)$ gives a good approximation to the residual ear canal component of the reflectance,

$$\widehat{\Gamma}_{mp}(s) \approx \Gamma_{\mathrm{TM}}(s). \tag{13}$$

Thus, from this factorization it is possible to estimate the normalized TM impedance using Eq. (1),

$$\frac{\widehat{Z}_{\mathrm{TM}}(s)}{r_0} = \frac{1+\widehat{\Gamma}_{mp}(s)}{1-\widehat{\Gamma}_{mp}(s)}. \tag{14}$$

When the approximate residual ear canal contribution has been removed, the magnitude TM impedance $|\widehat{Z}_{\mathrm{TM}}(j\omega)|/r_0$ typically has no high frequency notch due to ear canal standing waves. In the case of a uniform ear canal area $A(x)$, the TM impedance estimate is similar to the 'propagated impedance' function described by Voss and Allen (1994), calculated by removing a pure delay from the reflectance.

3. Results

3.1. Factorization of $\widehat{\Gamma}(s)$

An example factorization is shown in Fig. 5 for a normal ear, subject #7 of Voss and Allen (1994). The fit was performed in the reflectance domain over 0.1–10 [kHz], yielding $N_p = 18$ and $N_z = 18$ with a MSE of −31.9 [dB]; approximately overlapping pole-zero pairs at $\omega/(2\pi) \approx 7.5$ [kHz] and $\omega/(2\pi) \approx 9$ [kHz] were removed, yielding a MSE of −31.5 [dB] and $N_p = 14$ and $N_z = 14$. Fig. 5a and b show the poles and zeros of the all-pass and minimum-phase components of $\widehat{\Gamma}(s)$, similar to Fig. 4a and b. Note again how the poles and zeros of $\widehat{\Gamma}_{ap}(s)$ (Fig. 5a) are symmetrically placed about the ω axis, such that the zero labeled a has a symmetrical counterpart at $-a^*$, and the poles and zeros at f, f^*, $-f^*$ and $-f$ are constrained by both complex conjugation and all-pass symmetry. Considering Fig. 5b, the pole-zero pairs labeled b, c, d and e correspond in frequency ($f = \omega/(2\pi)$) to minima of the magnitude reflectance, as labeled in Fig. 5c. The first pair, labeled b, is located at about 1 [kHz], corresponding to the first minimum of the magnitude reflectance. This is similarly located to the pole-zero pair at a in Fig. 4b, which corresponds to the first minimum of the B&K 4157 magnitude reflectance in Fig. 1a; it is aligned with the low frequency edge of the broad minimum in $|\Gamma(\omega)|$ for average normal ears. While the B&K 4157 reflectance fit has an approximately flat magnitude from 1 to 4 [kHz] and has no more pole-zero pairs in this region, the reflectance fit for Voss and Allen subject #7 has closely spaced pole-zero pairs at c, d and e that correspond to the individually varying minima and maxima of its magnitude in that frequency region.

The total phase and the phases of the all-pass and minimum-phase components of the reflectance fit are shown in Fig. 5d. The phase of $\widehat{\Gamma}_{ap}(j\omega)$ appears linear, while the phase of $\widehat{\Gamma}_{mp}(j\omega)$ appears flatter than $\angle\widehat{\Gamma}(j\omega)$, meaning it contains less delay from the residual ear canal. This is apparent in the group delay as well, shown in Fig. 7a for the reflectance fit and its all-pass and minimum-phase components. The group delay of the all-pass component of the reflectance appears constant, with a value equal to the gap between the curves for the original reflectance fit and its minimum-phase component. Because the phase of the all-pass component is approximately linear (its group delay is approximately constant), the canal delay may be estimated by Eq. (12). For subject #7 (Voss and Allen, 1994), the group delay of $\widehat{\Gamma}_{ap}(j\omega)$ has a mean value across frequency of $\overline{\tau}_{ap} = 40.4$ [μs], with a standard deviation of 0.5 [μs]. Taking $\widehat{L} = \overline{\tau}_{ap}c/2$ with $c = 350$ [m/s], the estimated residual canal length $\widehat{L}$ is 7.1 [mm]; taking $\min(\tau_{ap}) = 38.9$ [μs], the estimated length is 6.8 [mm]. These are reasonable estimates, given that Voss and Allen estimate the length of the foam plug plus probe at 15 [mm], and the typical total ear canal length between the opening and center of the TM is about 23.5 [mm] (Fletcher, 1925). The TM impedance and phase are shown in Fig. 5e and f. Removing the all-pass component from the reflectance fit $\widehat{\Gamma}(s)$ removes the deep notch in the impedance magnitude ($|\widehat{Z}_{\mathrm{TM}}(j\omega)|/r_0$ does not have a high frequency notch), and causes the impedance phase to have no jump at the $|Z(\omega)|$ notch frequency.

A second example factorization is shown in Fig. 6. This is cadaver ear 12R from the Voss et al. (2012) study, in its normal (unmodified) state. The fit was performed in the reflectance domain over 0.2–6 [kHz], yielding $N_p = 12$ and $N_z = 12$ with a MSE of −35.8 [dB]. Fig. 6a and b show the poles and zeros of the all-pass and minimum-phase components of $\widehat{\Gamma}(s)$. Considering Fig. 6b, the pole-zero pairs labeled b, c, d and e correspond in frequency to minima of the magnitude reflectance labeled in Fig. 6c. The pole-zero pair labeled b is located at $\omega/(2\pi) = 1$ [kHz], corresponding to the first minimum of $|\widehat{\Gamma}(j\omega)|$ (similar to Voss and Allen subject #7 and the B&K 4157 ear simulator), and the pole-zero pairs at c and d correspond to the individually varying minima and maxima in the mid-frequency region of the magnitude reflectance. The pole-zero pair at a seems to correspond to a small bend in the reflectance below 1 [kHz]; presumably, it has a smaller effect on $|\widehat{\Gamma}(j\omega)|$ because it has more damping than the pairs at b and c, and the pole and zero are closer to overlapping than the pair at d. The tightly spaced pair labeled e corresponds to a small dip in a noisy region of the magnitude reflectance between 5 and 6 [kHz].

The total phase and the phases of the all-pass and minimum-phase components of the reflectance fit are shown in Fig. 6d for ear 12R from Voss et al. (2012). Here the all-pass component phase $\angle\widehat{\Gamma}_{ap}(j\omega)$ appears to have a frequency dependent delay.

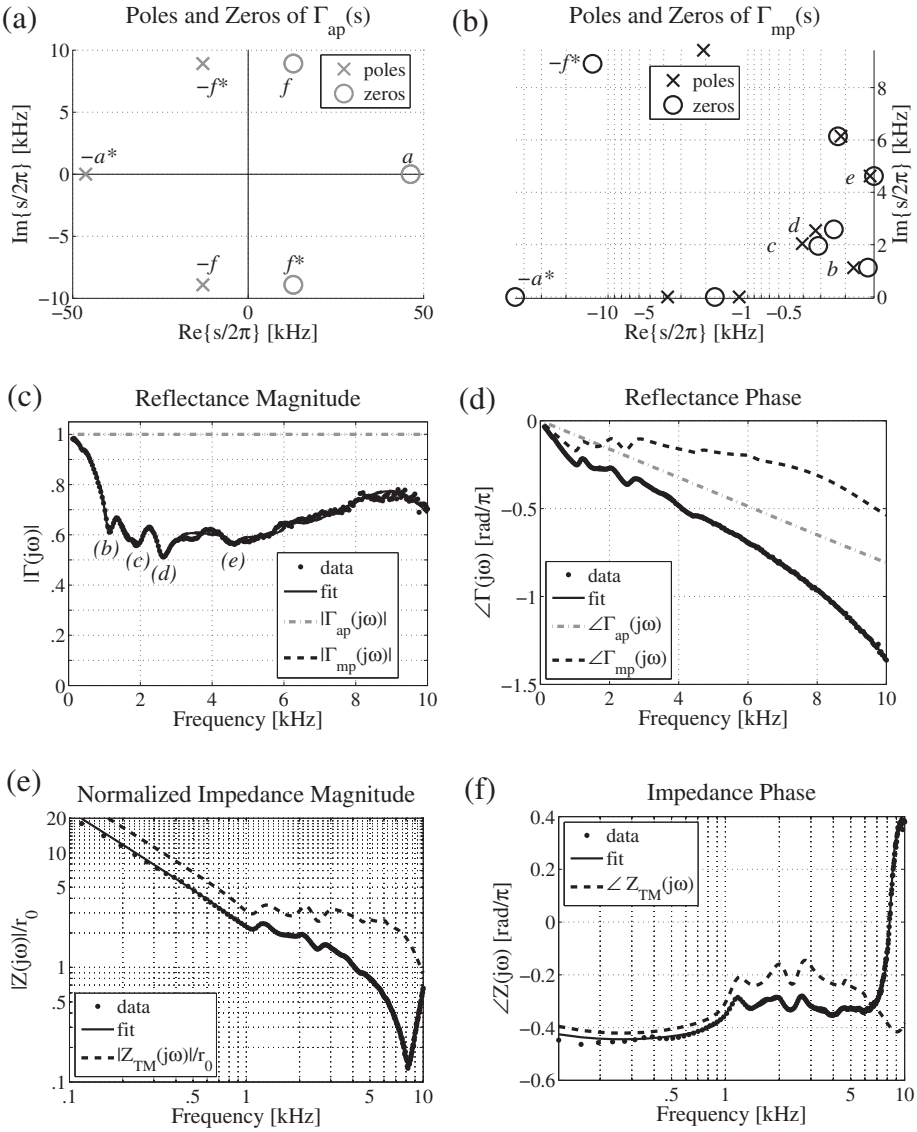

Fig. 5. Factored reflectance fit for subject #7 from Voss and Allen (1994). (a) Poles and zeros of $\hat{\Gamma}_{ap}(s)$, (b) poles and zeros of $\hat{\Gamma}_{mp}(s)$, (c) reflectance magnitude $|\hat{\Gamma}(j\omega)|$, (d) reflectance phase $\angle\hat{\Gamma}(j\omega)$, (e) normalized impedance magnitude $|\hat{Z}(j\omega)|/r_0$, (f) impedance phase $\angle\hat{Z}(j\omega)$. Note that $\hat{\Gamma}_{mp}(s)$ has no poles or zeros in the right half s-plane, thus the fit is completely described by northwest quadrant of the s-plane (shown in (b)). The fit was performed in the reflectance domain over 0.1–10 [kHz], yielding $N_p = 18$ and $N_z = 18$ with a RMS relative error of 2.5% (MSE = −31.9 [dB]); approximately overlapping pole-zero pairs at $\omega/(2\pi) \approx 7.5$ [kHz] and $\omega/(2\pi) \approx 9$ [kHz] were removed, yielding $N_p = 14$ and $N_z = 14$ with a MSE of −31.5 [dB].

Considering Fig. 6e and f, neither the approximated TM impedance $\hat{Z}_{TM}(j\omega)/r_0$ nor the data $Z(\omega)/r_0$ show a standing wave notch in the magnitude impedance, or a jump in the phase at high frequencies. This behavior is indicative of a very short ear canal distance between the probe tip and the TM. The magnitude estimated TM impedance $\hat{Z}_{TM}(j\omega)/r_0$ is relatively large at high frequencies in comparison with Fig. 5e; however, this seems plausible because the magnitude reflectance of the cadaver ear (Fig. 6c) is much closer to 1 at high frequencies than the magnitude reflectance of the normal ear (Fig. 5c, Voss and Allen subject #7).

Unlike measurements made in vivo, CAR measurements of cadaver ears typically have a much shorter residual ear canal, due to the nature of the preparation. For this ear, the group delay of the reflectance all-pass component, shown in Fig. 7b, is not constant. For Voss et al. (2012) ear 12R the mean group delay is 34.0 [μs] over the entire frequency range of the fit, with a standard deviation of 12.2 [μs]. Instead, a frequency independent group delay, estimated as the minimum value of the group delay of $\hat{\Gamma}_{ap}(j\omega)$ over the 0.2–6 [kHz] range ($\min(\tau_{ap}) = 21.7$ [μs]), yields the estimate $\hat{L} \approx 3.8$ [mm]. This is short compared to $\hat{L}$ for the in vivo measurement in the preceding example, which makes sense given the measurement conditions for cadaver ears. Variation of the all-pass group delay with frequency may be accounted for by non-uniform area of the ear canal, or lossless mass-stiffness properties of the TM and middle ear. The TM in particular may contribute a significant amount of lossless delay (Puria and Allen, 1998; Parent and Allen, 2010).

Estimating the residual ear canal length from the all-pass factor of the reflectance fit, the probe-TM distance for the B&K 4157 and DB-100 ear simulators are estimated to be 7.6 [mm] and 2.3 [mm], respectively. Considering Fig. 1, these results are reasonable, and agree with the observations made in Section 1.2. While the B&K 4157 shows large residual canal effects in the magnitude impedance and reflectance phase, the DB-100 does not. With a shorter probe-TM distance, the standing wave impedance notch for the DB-100 would be at a higher frequency than that for the B&K 4157,

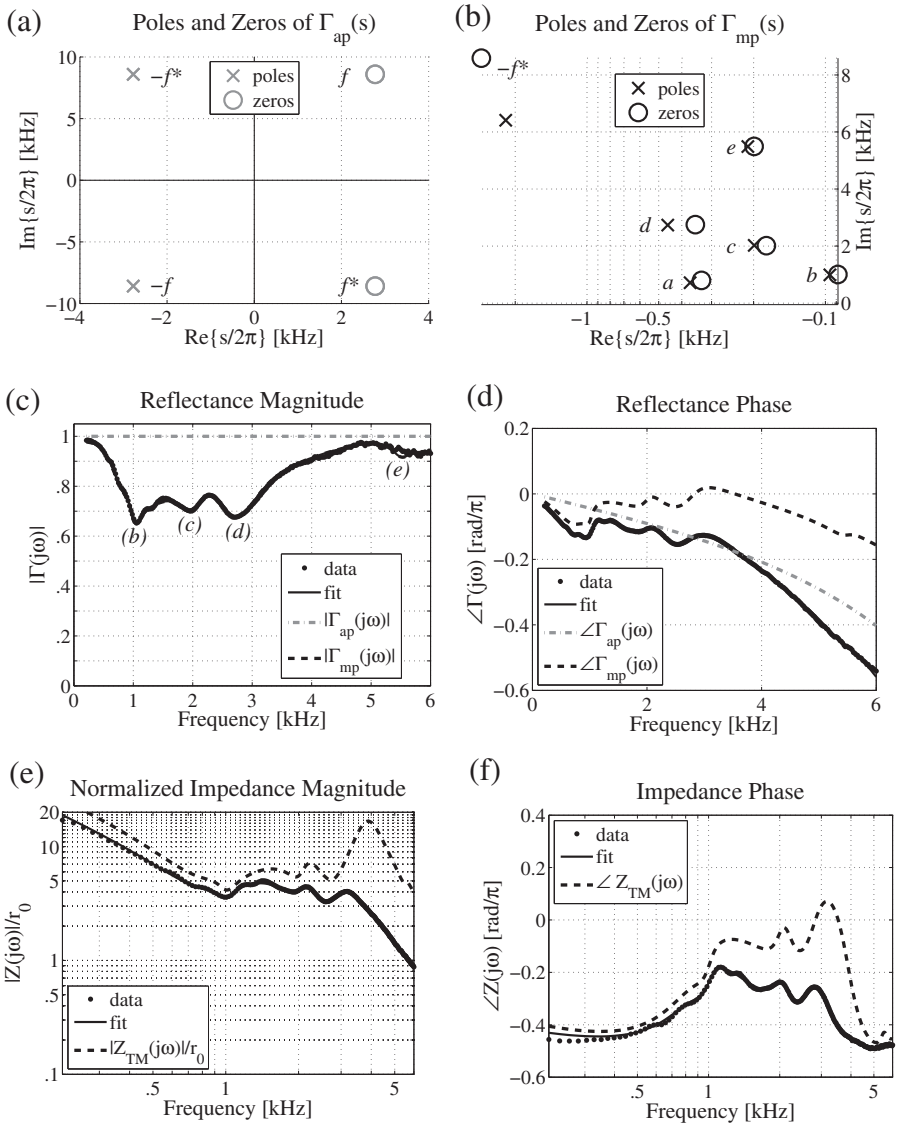

Fig. 6. Factored reflectance fit for cadaver ear 12R from Voss et al. (2012). (a) Poles and zeros of $\widehat{\Gamma}_{ap}(s)$, (b) poles and zeros of $\widehat{\Gamma}_{mp}(s)$, (c) reflectance magnitude $|\widehat{\Gamma}(j\omega)|$, (d) reflectance phase $\angle\widehat{\Gamma}(j\omega)$, (e) normalized impedance magnitude $|\widehat{Z}(j\omega)|/r_0$, (f) impedance phase $\angle\widehat{Z}(j\omega)$. Note that $\widehat{\Gamma}_{mp}(s)$ has no poles or zeros in the RHP, thus the fit is completely described by northwest quadrant of the s-plane (shown in (b)). The fit was performed in the reflectance domain over 0.2 to 6 [kHz], yielding $N_p = 12$ and $N_z = 12$ with a MSE of −35.8 [dB].

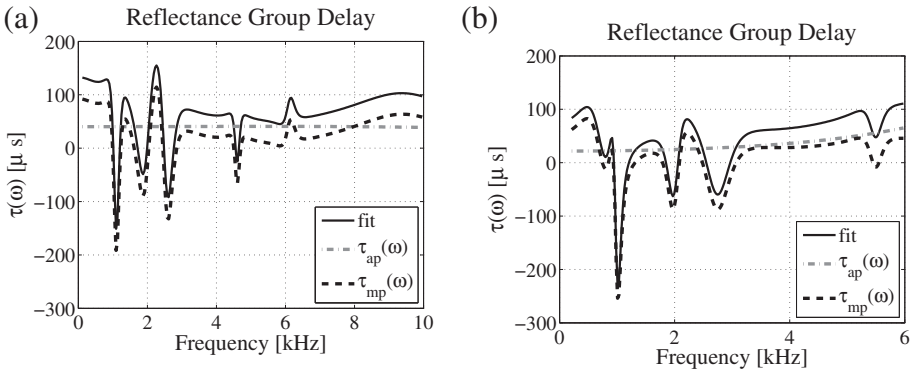

Fig. 7. Group delay of the fit $\widehat{\Gamma}(j\omega)$, and its factors $\widehat{\Gamma}_{mp}(j\omega)$ and $\widehat{\Gamma}_{ap}(j\omega)$. (a) Voss and Allen (1994) subject #7 from Fig. 5, (b) Voss et al. (2012) cadaver ear 12R ('normal' unmodified state) from Fig. 6. In (a), $\widehat{\Gamma}_{ap}(j\omega)$ has an approximately constant group delay; in (b), $\widehat{\Gamma}_{ap}(j\omega)$ has a frequency dependent group delay.

outside of the range shown. Additionally, the shorter canal of the DB-100 simulator requires the probe tip to be much closer to the middle ear (TM) for a good acoustic seal.

3.2. Characterization of CAR data

Figs. 8 and 9 show data and pole-zero fits of four reflectance measurements of ears with varying middle ear conditions (one normal + three pathologies). Fig. 8 shows a reflectance summary, while Fig. 9 shows a sensitivity analysis of various poles and zeros for each measurement. These poles and zeros were chosen to help the reader develop an intuition for the effect of pole-zero locations on the magnitude response. This exercise is meant as a tour of the pole-zero fits for various pathologies; two poles, zeros, or pole-zero pairs are chosen for each pathology, but any poles and zeros of the fit could be analyzed in this way.

Fig. 8b shows the *absorbance level* in [dB] (Allen et al., 2005; Rosowski et al., 2012), defined as

$$\text{Absorbance[dB]} \equiv 10\ \log_{10}\left(1-|\Gamma(\omega)|^2\right), \tag{15}$$

where $1-|\Gamma(\omega)|^2$ is the power absorbance. The mean and normative region of the absorbance level for normal middle ears have a very distinct shape. Rosowski et al. (2012) characterize the rising slope as 15 [dB] per decade and the falling slope as −23 [dB] per decade, with a flat region occurring between about 1 and 4 [kHz]. This is a useful way to characterize reflectance data, because deviations of the absorbance level from normal are more easily recognized, and are closely related to hearing sensitivity (Allen et al., 2005). Additionally, the absorbance level condenses in a rational way the region of individual variation in the magnitude reflectance for normal ears, to a range of a few [dB].

Fig. 9 is comprised of four subplots. In each subplot, the left panel shows two sensitivity analyses of poles and zeros from the right panel; different analyses are color-coded in red and blue. These color-coded regions display ratios of a modified magnitude reflectance fit to the original $|\widehat{\Gamma}_{mp}(j\omega)|$, shown in Fig. 8a for each of the four measurements, as a function of frequency. Note that the frequency axes of the left and right panels in each subplot are vertically aligned. For each sensitivity analysis, the reflectance is modified by shifting the color-coded pole, zero, or pole-zero pair of $\widehat{\Gamma}_{mp}(s)$ by 10% of its value on the s plane; pole-zero pairs are shifted as a unit about their two-dimensional centers. Sensitivity regions show the minimum and maximum values of the ratio

$$R_\Gamma(\omega) = \frac{\left|\widehat{\Gamma}_{mp}(s+\varepsilon(s))\right|_{s=j\omega}}{\left|\widehat{\Gamma}_{mp}(s)\right|_{s=j\omega}} \tag{16}$$

out of 1000 shifts of the chosen pole, zero, or pair (s_k) by

$$\varepsilon(s) = \begin{cases} 0.1\left|\dfrac{1}{N}\displaystyle\sum_{k=1}^{N} s_k\right| e^{j\Theta} & \text{for } s = s_k \\ 0 & \text{else} \end{cases} \tag{17}$$

where Θ is a random variable uniformly distributed between $-\pi$ and π.

A sensitivity analysis is presented in Fig. 9 for a normal ear (Fig. 8 black, Fig. 9a) from Rosowski et al. (2012) and for three pathological ears from Nakajima et al. (2012). A representative measurement has been chosen for each pathology examined in that study, including stapes fixation (Fig. 8 orange, Fig. 9b), ossicular disarticulation (Fig. 8 purple, Fig. 9c), and *superior semicircular canal dehiscence* (SSCD) (Fig. 8 green, Fig. 9d).

3.2.1. Normal ears

Consider the normal ear measurement shown in Fig. 8, ear 22L of the Rosowski et al. (2012) study of normal ears. This fit was performed on reflectance domain data with E forced to zero, achieving a MSE of −35.6 [dB] with 12 poles and 12 zeros. The resulting poles and zeros of $\widehat{\Gamma}_{mp}(s)$ are shown in Fig. 9a (right). The magnitude reflectance $|\widehat{\Gamma}_{mp}(j\omega)| = |\widehat{\Gamma}(j\omega)|$ is plotted in Fig. 8a (black). Normative data, showing ±1 standard deviation for 112 measurements of normal ears (Rosowski et al., 2012), is plotted as the shaded gray region in Fig. 8a and b; ear 22L falls within this normal region.

Considering Fig. 9a (left), the red shaded region shows a sensitivity analysis of the pole-zero pair labeled *a* at about 900 [Hz] (close to 1 [kHz]), and the blue region shows a sensitivity analysis of the pole-zero pair labeled *b* at 2.5 [kHz]. These pole-zero pairs were analyzed because they lie in the mid-frequency region, where normal ears show individually varying minima and maxima of the magnitude reflectance. Note that the frequency axis of the sensitivity plot is aligned with that of the pole–zero plot for comparison. According to Fig. 9a (left), the reflectance magnitude is only significantly affected by variations of the pair location in the frequency neighborhood where each pair resides. This indicates that the exact location and curvature of the minima and maxima in those frequency regions are determined by the corresponding pole-zero pairs.

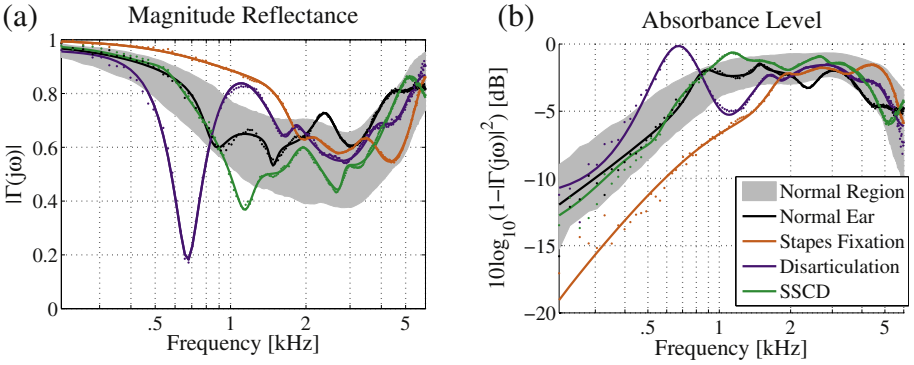

Fig. 8. Magnitude reflectance and absorbance level of one normal and three pathological ears. (a) Magnitude reflectance $|\widehat{\Gamma}(j\omega)|$, (b) absorbance level $10\log_{10}\left(1-|\widehat{\Gamma}(j\omega)|^2\right)$ [dB]. The gray region shows normative data from the Rosowski et al. (2012) study of normal ears (±1 standard deviation). The black dots and lines show the raw data and fit for normal ear 22L from Rosowski et al. (2012). The orange, purple, and green dots and lines show the data and fit for stapes fixation ear 62L, disarticulation (ossicular discontinuity) ear 28L, and SSCD ear 52L from Nakajima et al. (2012).

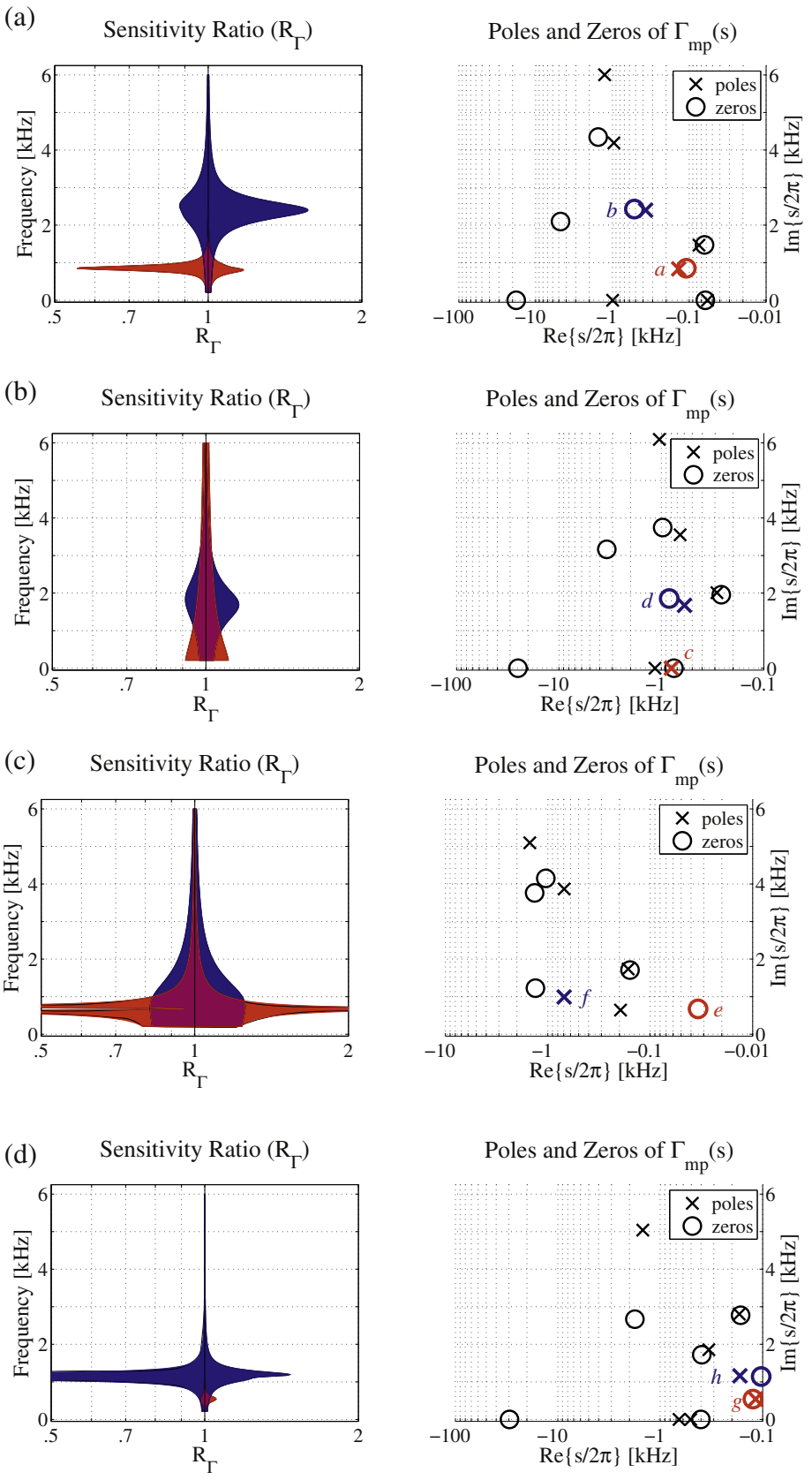

Fig. 9. Sensitivity analysis of select poles and zeros for the ears of Fig. 8. Each subplot shows the pole–zero plot of $\hat{\Gamma}_{mp}(s)$ (right), and two color-coded sensitivity analyses corresponding to the highlighted poles and zeros (left); the frequency axes are vertically aligned for each pair of plots. (a) Normal ear, (b) stapes fixation, (c) disarticulation, (d) SSCD. Each sensitivity analysis shows the minimum and maximum values of R_Γ (Eq. (16)) across frequency for the corresponding colored pole, zero, or pole-zero pair.

Thus, the individually varying fine-structure minima and maxima in the 1–5 [kHz] range (Allen et al., 2005; Rosowski et al., 2012) seem to be characterized primarily by closely-associated pole-zero pairs in that frequency range. Identifying the pole-zero behavior that characterizes the variation of normal ears will allow for better detection of abnormal reflectance measurements. Additionally, the pole-zero pair located close to 1 [kHz] corresponds to the first minimum of $|\widehat{\Gamma}(j\omega)|$ and the 'breakpoint' of the power absorbance (Fig. 8b), between the low-frequency ramp and the flat region. Based upon the pole-zero fits for this ear, the B&K 4157 (Fig. 4b), Voss and Allen (1994) subject #7 (Fig. 5b), and Voss et al. (2012) cadaver ear 12R (Fig. 6b), it seems that $\widehat{\Gamma}_{mp}(s)$ for normal ears will typically have pole-zero pair near 1 [kHz], characterizing the breakpoint of the absorbance level (and the first minimum of the magnitude reflectance).

3.2.2. Stapes fixation

The orange fit curve and data points in Fig. 8a and b show an example CAR measurement (patient ear 62L, Nakajima et al. (2012)) for a patient with confirmed stapes fixation due to otosclerosis, in the presence of an intact TM and aerated middle ear. The reflectance domain fit has $N_p = 10$, $N_z = 10$, and a MSE of −40.3 [dB]. The absorbance level (Fig. 8b) and magnitude reflectance (Fig. 8a) for this ear fall significantly outside of the normative regions.

Stapes fixation due to otosclerosis is best characterized by an increased middle ear stiffness (Feeney et al., 2003; Allen et al., 2005; Nakajima et al., 2012). This typically results in an elevated reflectance magnitude at low frequencies, corresponding to a right shift of the low-frequency sloping region of the absorbance level (Allen et al., 2005). This behavior is apparent in Fig. 8b, where the absorbance level curve for ear 62L is significantly shifted to the right of the normative region below 2 [kHz]. The sensitivity plot in Fig. 9b (left) analyzes low frequency singularities, due to the unusual behavior of the magnitude reflectance at low frequencies.

The red region of Fig. 9b (left) shows a sensitivity analysis of the pole labeled *c* on the real axis of $\widehat{\Gamma}_{mp}(s)$, closest to the origin. This pole was chosen because it has the least damping, thus the strongest effect on the reflectance, and the magnitude reflectance is higher (has a more pole-like behavior) at low frequencies. The movement of this pole affects the magnitude reflectance at low frequencies up to about 2 [kHz]. Moving this pole towards the origin strengthens its effect, increasing the magnitude reflectance at low frequencies, and moving it away from the origin will decrease the magnitude reflectance at low frequencies. The blue region shows the sensitivity analysis for the pole-zero pair labeled *d* at about 1.75 [kHz]. This pair was chosen because it is the first pole, zero, or pair occurring in frequency off the σ axis, when we would expect to see a pole-zero pair at about 1 [kHz] for a normal ear. While its largest effect occurs in the frequency neighborhood where the pair resides, movement of this pole-zero pair also affects the magnitude reflectance at low frequencies. This pair appears to characterize the breakpoint of the absorbance level (and perhaps also, in part, its slope) for this pathological ear. For normal ears, this breakpoint occurs significantly lower in frequency, around 1 [kHz], as discussed in Section 3.2.1.

3.2.3. Ossicular discontinuity

The purple fit curve and data points in Fig. 8a and b show an example CAR measurement (patient ear 28L, Nakajima et al. (2012)) for a patient with confirmed ossicular discontinuity, in the presence of an intact TM and aerated middle ear. The reflectance domain fit has $N_p = 10$, $N_z = 10$, and a MSE of −31.3 [dB]. The absorbance level (Fig. 8b) and magnitude reflectance (Fig. 8a) for this ear also fall outside the normative regions, but the nature of this variation is quite different from that due to stapes fixation.

Ossicular discontinuity typically causes a narrow-band (tuned) resonance in the magnitude reflectance between 0.5 and 0.8 [kHz] (Nakajima et al., 2012). This is visible in the case of ear 28L, which has a deep notch in the reflectance magnitude at about 700 [Hz] and a corresponding elevated absorbance level in that frequency region. The absorbance level does not have a normal breakpoint at 1 [kHz]. The poles and zeros of $\widehat{\Gamma}_{mp}(s)$ correspondingly show an abnormal behavior in this range. In this case of ossicular discontinuity there are poles and zeros near 1 [kHz], but they are not tightly paired. Hence, the pole and zero closest in frequency to 1 [kHz] are analyzed.

Fig. 9c (left) shows a sensitivity analysis of the poles and zeros close to 1 [kHz]. The red region indicates that the zero labeled *e* near 700 [Hz] characterizes the deep notch in the magnitude reflectance. The magnitude reflectance is very sensitive to the location of this zero, experiencing sharp relative dips when it is moved higher or lower in frequency. It makes sense that this zero has a large effect on the magnitude response, because it has a very small σ value compared to the other poles and zeros of $\widehat{\Gamma}_{mp}(s)$. The blue region shows the sensitivity of the magnitude reflectance to the pole labeled *f* at 1 [kHz]. Not only does this pole affect the magnitude reflectance in the 1 [kHz] region (where the magnitude reflectance is higher than average), but it has a significant effect on the magnitude reflectance for all frequencies below 2 [kHz].

3.2.4. Superior semicircular canal dehiscence (SSCD)

The green fit curve and data points in Fig. 8a and b show an example CAR measurement (patient ear 52L, Nakajima et al. (2012)) for a patient with confirmed SSCD, in the presence of an intact TM and aerated middle ear. The reflectance domain fit has $N_p = 12$, $N_z = 12$, and an MSE of −34.3 [dB]. The absorbance level (Fig. 8b) and magnitude reflectance (Fig. 8a) for this ear fall slightly outside of the normative regions around 1 [kHz].

SSCD typically shows a similar variation from normal to that caused by ossicular discontinuity, though not as extreme (Nakajima et al., 2012). In Fig. 8a there is an abnormally deep minimum in the magnitude reflectance at 1 [kHz], corresponding to a slight elevation of the absorbance level at that frequency (Fig. 8b), relative to the normal middle ear region. Comparing this with the purple curve for ossicular discontinuity, the effect is similar but not as pronounced, and the notch occurs in a slightly higher frequency range. Because the variation in the magnitude reflectance is observed at low frequencies around 1 [kHz], the sensitivity of poles and zeros in that region is analyzed.

Fig. 9d (left) shows the sensitivity analysis for the pole-zero pairs at 500 [Hz] and 1 [kHz] in Fig. 9d (right). The red region of Fig. 9d (left) shows the effect of the pole-zero pair labeled *g* at 500 [Hz] on the magnitude reflectance. This pair was selected because it lies between the σ axis and the normal 1 [kHz] pair location. Shifting this pole-zero pair causes a variation in the reflectance magnitude around that frequency. However, the effect is not very pronounced; the pole and zero are very close together, and appear to be fitting a small noise peak. In fact, this effect is so small compared to the effect of the 1 [kHz] pole-zero pair, that the red region is hard to see. The blue region shows that shifting the pole-zero pair labeled *h* at 1 [kHz] causes large variations of the magnitude reflectance in that frequency neighborhood. Notice that the zero of this pair has a significantly smaller σ value than the pole, increasing its relative effect on the reflectance. This zero and its distance from the pole affect the depth of the minimum in the magnitude reflectance at 1 [kHz]. This pole-zero pair also characterizes the nature of the breakpoint in the absorbance level between the initial slope and the flat region. Considering the pole-zero pairs near 1 [kHz] found for normal ears in this paper (Figs. 4b, 5b, 6b and 9a (right)), the abnormal depth of the 1 [kHz] notch in the SSCD magnitude reflectance could be due to

nuances of the location of its 1 [kHz] pair, such as damping and relative distance between the pole and zero.

4. Discussion

4.1. Limitations

The pole-zero fitting method is limited by the data provided, and will typically not be accurate outside of the fitted frequency range (either above or below). Because the reflectance is not known at higher or lower frequencies, the calculation of $\widehat{\Gamma}_{ap}(s)$, approximating the residual ear canal effect, must be inherently imperfect (Voss and Allen, 1994). Additionally, the appropriate relative order of the fit (N_z vs. N_p) is related to high frequency asymptotic behavior of the data, which may be unknown. As stated in Section 2.1, the relative order is determined by the values of D and E in Eq. (5); these fit the high frequency data, because all other terms (e.g. $C_i/(s - A_i)$) go to zero for large ω values.

Pole-zero fits to the data are also impacted by the estimated surge resistance r_0 (Eq. (1)). The use of an incorrect area value to calculate r_0 will cause errors in the calculation of the reflectance (Rasetshwane et al., 2012). For the Mimosa Acoustics HearID system, the canal area A is set according to the size of the foam tip used. It has been shown that small variations in the ear canal area relative to the calibration cavity area, within 20%, cause a negligible change in the reflectance measurement (Keefe et al., 1992; Voss and Allen, 1994). Nonetheless, this will have a small effect on the CAR function and the pole-zero locations of its approximation.

4.2. Relative order of $\widehat{\Gamma}(s)$

In Section 2.1.2, it was determined empirically that the fit parameter E should be set to zero when fitting in the reflectance domain, while the value D should not (though it is typically small). When E is forced to zero, the inverse Laplace transform of the reflectance fit $\widehat{\Gamma}(s)$ is

$$\widehat{\gamma}(t) = D\delta(t) + \sum_{i=1}^{N_p} C_i e^{A_i t} u(t). \tag{18}$$

Thus, a non-zero fit parameter D corresponds to an initial Dirac δ-function singularity of the time domain reflectance (Lundberg et al., 2007); this value D is related to the reflectance fit via

$$\lim_{\sigma \to +\infty} \left[\widehat{\Gamma}(s)\right] = D. \tag{19}$$

Now consider the surge resistance, which is defined as the initial δ-function singularity of the time domain impedance (Section 1.1). For a transmission line model of the ear canal and middle ear (e.g. having wave propagation) the impedance $Z(s)$ at the probe tip has the property

$$\lim_{\sigma \to +\infty} [Z(s)] = \bar{r}_0, \tag{20}$$

where $\bar{r}_0$ is the true surge resistance, a real-valued constant. Considering Eq. (1) in this limit, we find

$$\lim_{\sigma \to +\infty} [\Gamma(s)] = \frac{\bar{r}_0 - r_0}{\bar{r}_0 + r_0}. \tag{21}$$

If r_0 is equal to the true surge resistance $\bar{r}_0$, the limit of $\Gamma(s)$ as $\sigma \to +\infty$ must be zero. This means there must be no initial δ-singularity in the time domain reflectance (Claerbout, 1985). Thus, considering Eqs. (19) and (21), D should be zero; a non-zero value of D may indicate a fitting inaccuracy, or the use of an incorrect r_0 value. In the latter case, if the fitting procedure yields a good approximation of the initial singularity in the time domain reflectance, due to an incorrect r_0 value, D might be used to estimate the true surge resistance value from the CAR data via

$$\overline{r_0} = r_0 \frac{1 + D}{1 - D}. \tag{22}$$

4.3. Applications

The fitting algorithm is fast, and may be easily implemented in a reflectance measurement system. Ultimately, it may allow for more robust automated classification than visual assessment or correlations between magnitude reflectance values and audiometric measurements. Pole-zero fitting is advantageous because it reduces the entire complex response to a small set of parameters, without extensive processing of the CAR data. Further study will be needed to meet this objective, using larger sets of normal and pathological CAR data in combination with known physical characteristics of normal and pathological middle ears, to establish final classification strategies.

Pole-zero fits may also be used to synthesize network models of the complex impedance (e.g. Brune, 1931; Van Valkenburg, 1964). However, such RLC networks will not necessarily be unique. Networks synthesized from pole-zeros fits of CAR measurements will often lack direct physical interpretations present in other models, such as the Zwislocki (1962), Kringlebotn (1988), or Parent and Allen (2010) models. However, they will have great utility for quantifying CAR data.

As stated in Section 1.1, pole-zero fits are not intended to be used in their raw form in the clinical realm; a visual diagnosis may be much better achieved by considering the absorbance level in [dB], as shown in Fig. 8b. However, we believe that this method is of great value for modeling and diagnosis of middle ear pathologies based on reflectance. Pole-zero fitting allows for a concise quantitative representation of reflectance that can be useful when designing algorithms to automatically detect pathologies.

4.4. Summary

This study establishes a methodology for examining the physical and mathematical properties of CAR data using pole-zero fitting. Pole-zero fits can characterize CAR data with low error and small number of parameters. While the complex data reintroduces measurement variation due to the residual ear canal, measurements may be effectively compared across ears by factoring the reflectance fit into its minimum-phase and all-pass components. The magnitude of the minimum-phase component of the CAR is, by definition, equal to the reflectance magnitude, thus preserving the current diagnostic standard. In this investigation, it was established that reflectance domain fits show distinct pole-zero pairs in the mid-frequency region of individual variation for normal ears, and that they may systematically differ for various pathologies. Pole-zero modeling provides a concise, parametric characterization of CAR data, in order to enable improved automated identification of middle ear pathology using a noninvasive, yet relatively low cost measurement system.

Acknowledgments

Many thanks to the Human Speech Recognition group at UIUC. This material is based upon work supported by the National Science Foundation under Grant No. 0903622, and NIH Bioengineering Research Partnership R01 EB013723, PI: Stephen Boppart.

Appendix A. Vector fitting

A vector fitting procedure developed by Gustavsen and Semlyen (1999) is used to fit complex, frequency domain data to a function of the form shown in Eq. (5). The vector fitting procedure is an iterative two step process, which converts a nonlinear least squares problem to a linear least squares problem by introducing an unknown scaling function Θ, having known poles. Let the iteration index of the algorithm be denoted by $m = 1,2,\ldots,M$. Note that the pole order of the algorithm is fixed; if some error criterion is not met, the algorithm may be re-run with a greater number of poles N_p. On each iteration, a least squares problem is solved based on the following equations:

$$H_m(s) = \sum_{i=1}^{N_p} \frac{c_{i,m}}{s - a_{i,m-1}} + d_m + e_m s \tag{A.1}$$

$$\Theta_m(s) = \sum_{i=1}^{N_p} \frac{b_{i,m}}{s - a_{i,m-1}} + 1. \tag{A.2}$$

These equations are linear in their unknowns $c_{i,m}$, d_m, e_m, and $b_{i,m}$. Both $\Theta_m(s)$ and $H_m(s)$ share the same known poles $a_{i,m-1}$, which have either been determined in the previous iteration, or initialized by the user. It is important that $\Theta_m(s)$ and $H_m(s)$ have the same poles, because the poles algebraically cancel when a ratio of the functions is taken in a later step of the algorithm (Eq. (A.4)). The algorithm iterates to converge on the unknown poles $A_i = a_{i,M}$ of the fit $\widehat{F}(s) = F_M(s)$ (which are a nonlinear unknown in Eq. (5)). The initial poles $a_{i,0}$ are the 'starting poles' of the algorithm; their selection will be described below.

The vector fitting method relates Eqs. (A.1) and (A.2) to the measured data $F(\omega_k)$ at a given frequency index k via

$$\Theta_m(s)|_{s=j\omega_k} F(\omega_k) = H_m(s)|_{s=j\omega_k}. \tag{A.3}$$

When evaluated over the many available frequency points of $F(\omega)$, Eq. (A.3) results in an over-determined linear problem in the unknowns $c_{i,m}$, d_m, e_m, and $b_{i,m}$. At each algorithm step, the current fit is given by

$$F_m(s) = \frac{H_m(s)}{\Theta_m(s)} \tag{A.4}$$

using the estimated values of $c_{i,m}$, d_m, e_m, and $b_{i,m}$. This fit is related to the data via

$$F(\omega) \approx F_m(s)|_{s=j\omega} \tag{A.5}$$

and should improve with iteration.

Because $H_m(s)$ and $\Theta_m(s)$ share the same poles, by construction there is a perfect cancellation in Eq. (A.4). Thus, upon iteration, the zeros of $\Theta_m(s)$ become the poles of $F_m(s)$. To see this, consider the product forms of Eqs. (A.1) and (A.2) for a non-zero e_m,

$$H_m(s) = \frac{e_m \prod_{i=1}^{N_p+1} (s - z_{i,m})}{\prod_{i=1}^{N_p} (s - a_{i,m-1})} \tag{A.6}$$

$$\Theta_m(s) = \frac{\prod_{i=1}^{N_p} (s - a_{i,m})}{\prod_{i=1}^{N_p} (s - a_{i,m-1})} \tag{A.7}$$

where $z_{i,m}$ are the zeros of $H_m(s)$, $a_{i,m}$ are the zeros of $\Theta_m(s)$, and $a_{i,m-1}$ are the known poles of both functions. Substituting Eqs. (A.6) and (A.7) for Eq. (A.4) yields

$$F_m(s) = \frac{H_m(s)}{\Theta_m(s)} = \frac{e_m \prod_{i=1}^{N_p+1} (s - z_{i,m})}{\prod_{i=1}^{N_p} (s - a_{i,m})}. \tag{A.8}$$

Thus, on each iteration the zeros of the scaling function $\Theta_m(s)$ become the poles of the fitted function $F_m(s)$. On the last iteration, the poles $a_{i,M}$ become the poles of $F_M(s) = \widehat{F}(s)$ (Eq. (5)) such that $A_i = a_{i,M}$. Gustavsen and Semlyen found that it is better to calculate the remaining quantities C_i, D, and E via the least squares procedure outlined by Eq. (A.3), using $a_{i,M}$ as the starting poles. Thus, the final quantities $C_i = c_{i,M+1}$, $D = d_{M+1}$, and $E = e_{M+1}$ are the result of a partial iteration.

An appropriate selection of starting poles $a_{i,0}$ is necessary for the convergence of the vector fitting method. For a function with resonance peaks, such as the reflectance, Gustavsen and Semlyen (1999) suggest that the starting poles (complex conjugate pairs $a_{i,0} = -\alpha_{i,0} \pm j\beta_{i,0}$, with $\alpha_{i,0} = \beta_{i,0}/100$ advised) be linearly distributed over the frequency range of the data. The linear problem can become ill-conditioned if the starting poles are real. Large differences between the starting poles and the best fit poles of the response can cause large differences between $\Theta_m(s)$ and $H_m(s)$ resulting in poor least squares solutions (Gustavsen and Semlyen, 1999).

If the least squares procedure returns unstable poles ($\mathrm{Re}\{a_{i,m}\} > 0$), their real parts are reflected to the left half s-plane before the next iteration. Due to this, the error will not always decrease monotonically with iteration. Depending on the application, it may also be beneficial to impose additional properties. For example, one might force the impedance to be minimum-phase, instead of merely stable. This could be done by inverting the real part of any zero that appears in the RHP, similar to the procedure for enforcing stability of the poles. Such a constraint may cause an increase in error, but could have utility for physical modeling.

The error depends on the starting pole values due to noise in the data. Additionally, due to the smoothness of the reflectance function and the number of available parameters, there exist multiple non-unique fits yielding reasonable fit errors (e.g. within a certain MSE tolerance). Thus the poles (of an already low error fit) may vary with iteration, resulting in non-monotonic error. Typically, significant MSE improvement over the first few iterations occurs only for low pole orders (e.g. $N_p < 10$ over a 0.1–10 [kHz] range). For high pole orders (e.g. $N_p > 20$ over the same range) the fitting procedure achieves close to its lowest MSE within one iteration. When the order is approximately known, as it is here, the starting poles better cover the entire frequency range, causing the fit to commonly converge within a few iterations. For low orders of poles, more iterations may be necessary to migrate the poles to their best fit locations.

References

Aibara, R., Welsh, J.T., Puria, S., Goode, R.L., 2001. Human middle-ear sound transfer function and cochlear input impedance. Hearing Research 152, 100–109.

Allen, J.B., 1986. Measurement of Eardrum Acoustic Impedance. In: Allen, J.B., Hall, J.L., Hubbard, A., Neely, S.T., Tubis, A. (Eds.), Peripheral Auditory Mechanisms. Springer-Verlag, New York, pp. 44–51.

Allen, J.B., Jeng, P.S., Levitt, H., 2005. Evaluation of human middle ear function via an acoustic power assessment. Journal of Rehabilitation Research & Development 42, 63–78.

Brune, O., 1931. Synthesis of a finite two-terminal network whose driving-point impedance is a prescribed function of frequency. Journal of Mathematical Physics 10, 191–236.

Campbell, G.A., 1922. Physical theory of the electric wave filter. Bell System Technical Journal 1, 1–32.
Claerbout, J., 1985. Imaging the Earth's Interior. Blackwell Scientific, Palo Alto, CA, pp. 287–289.
Farmer-Fedor, B.L., Rabbitt, R.D., 2002. Acoustic intensity, impedance and reflection coefficient in the human ear canal. The Journal of the Acoustical Society of America 112, 600–620.
Feeney, M.P., Grant, I.L., Marryott, L.P., 2003. Wideband energy reflectance measurements in adults with middle-ear disorders. Journal of Speech, Language, and Hearing Research 46, 901–911.
Fletcher, H., 1925. Useful numerical constants of speech and hearing. Bell System Technical Journal IV, 375–386.
Gustavsen, B., Semlyen, A., 1999. Rational approximation of frequency domain responses by vector fitting. IEEE Transactions on Power Delivery 14, 1052–1061.
Hunter, L.L., Feeney, M.P., Lapsley Miller, J.A., Jeng, P.S., Bohning, S., 2010. Wideband reflectance in newborns: normative regions and relationship to hearing-screening results. Ear and Hearing 31, 599–610.
Keefe, D.H., Ling, R., Bulen, J.C., 1992. Method to measure acoustic impedance and reflection coefficient. The Journal of the Acoustical Society of America 91, 470–485.
Kringlebotn, M., 1988. Network model for the human middle ear. Scandinavian Audiology 17, 75–85.
Lundberg, K.H., Miller, H.R., Trumper, R.L., 2007. Initial conditions, generalized functions, and the Laplace transform: troubles at the origin. IEEE Control Systems Magazine 27, 22–35.
Nakajima, H.H., Pisano, D.V., Roosli, C., Hamade, M.A., Merchant, G.R., Mahfoud, L., Halpin, C.F., Rosowski, J.J., Merchant, S.N., 2012. Comparison of ear-canal reflectance and umbo velocity in patients with conductive hearing loss: a preliminary study. Ear and Hearing 33, 35–43.
Parent, P., Allen, J.B., 2010. Time-domain "wave" model of the human tympanic membrane. Hearing Research 263, 152–167.
Puria, S., Allen, J.B., 1998. Measurements and model of the cat middle ear: evidence of tympanic membrane acoustic delay. The Journal of the Acoustical Society of America 104, 3463–3481.
Rasetshwane, D.M., Neely, S.T., Allen, J.B., Shera, C.A., 2012. Reflectance of acoustic horns and solution of the inverse problem. The Journal of the Acoustical Society of America 131, 1863–1873.
Recio-Spinoso, A., Fan, Y., Ruggero, A., 2011. Basilar-membrane responses to broadband noise modeled using linear filters with rational transfer functions. IEEE Transactions on Biomedical Engineering 58, 1456–1465.
Rosowski, J.J., Mehta, R.P., Merchant, S.N., 2003. Diagnostic utility of laser-doppler vibrometry in conductive hearing loss with normal tympanic membrane. Otology & Neurotology 24, 165–175.
Rosowski, J.J., Nakajima, H.H., Hamade, M.A., Mahfoud, L., Merchant, G.R., Halpin, C.F., Merchant, S.N., 2012. Ear-canal reflectance, umbo velocity, and tympanometry in normal-hearing adults. Ear and Hearing 33, 19–34.
Rosowski, J.J., Nakajima, H.H., Merchant, S.N., 2008. Clinical utility of laser-doppler vibrometer measurements in live normal and pathologic human ears. Ear and Hearing 29, 3–19.
Scheperle, R.A., Neely, S.T., Kopun, J.G., Gorga, M.P., 2008. Influence of in situ, sound-level calibration on distortion-product otoacoustic emission variability. The Journal of the Acoustical Society of America 124, 288–300.
Van Valkenburg, M.E., 1964. Modern Network Synthesis. John Weily & Sons, Inc., New York, NY.
Voss, S.E., Allen, J.B., 1994. Measurement of acoustic impedance and reflectance in the human ear canal. The Journal of the Acoustical Society of America 95, 372–384.
Voss, S.E., Horton, N.J., Woodbury, R.R., Sheffield, K.N., 2008. Sources of variability in reflectance measurements on normal cadaver ears. Ear and Hearing 29, 651–665.
Voss, S.E., Merchant, G.R., Horton, N.J., 2012. Effects of middle-ear disorders on power reflectance measured in cadaveric ear canals. Ear and Hearing 33, 195–208.
Voss, S.E., Rosowski, J.J., Merchant, S.N., Peake, W.T., 2000. Acoustic responses of the human middle ear. Hearing Research 150, 43–69.
Withnell, R.H., Jeng, P.S., Waldvogel, K., Morgenstein, K., Allen, J.B., 2009. An in situ calibration for hearing thresholds. The Journal of the Acoustical Society of America 125, 1605–1611.
Zwislocki, J., 1962. Analysis of the middle-ear function. part I: input impedance. The Journal of the Acoustical Society of America 34, 1514–1523.